# Combining optical ray tracing and acoustical finite elements for the simulation and optimization of a photoacoustic cell

Péter Rucz[1,2], Judit Angster[1], Agnes Sophia Meidert[3], Gustav Schelling[3], András Miklós[1]
[1] *Fraunhofer Institute for Building Physics, 70569 Stuttgart, Germany*
[2] *Budapest University of Technology and Economics, 1111 Budapest, Hungary, Email: rucz@hit.bme.hu*
[3] *LMU Klinikum, Clinic for Anesthesiology, 81377 München, Germany*

## Introduction

Photoacoustical trace gas analysis exploits the photoacoustic (PA) phenomenon for the measurement of the concentration of different gas species. An attractive property of this techinique is that the magnitude of the useful signal is linearly proportional to the concentration of the trace gas in the sample over many orders of magnitude [1]. By using an acoustical resonator, the signal to noise ratio can be enhanced enabling detection in the order of parts per billion (ppb) concentrations.

This paper discusses the application of optical ray tracing (RT) and the acoustical finite element (FE) method in the design of a photoacoustic cell for the detection of the anesthetic agent propofol in the expired air. First, the concept of a differential detector that enables the simultaneous detection of propofol and acetone is introduced. Then, the optical subsystem of the cell is simulated by means of geometrical ray tracing. The FE model of the cell includes the photoacoustic excitation computed using the RT simulation and a treatment of viscothermal losses at the walls. Optimization of the geometry is performed using the computational model. Finally, the simulation results are compared to measurements.

## Differential PA detector

The detection of propofol in the exhaled air involves various challenges. First, previous studies indicate that a concentration of a few ppb can be expected [2]. Second, in order to avoid water vapor condensation in the cell the cell must be heated to a temperature of 90–120 °C. While heating the cell also reduces the adsorption of molecules to the inner surfaces, it makes mounting the microphones directly to the walls infeasible. Third, the presence of acetone in the breath makes the direct measurement of propofol impossible, as both gases absorb light in the same range of wavelengths. Based on the data published by Laurila *et al.* [3], Figure 1(a) displays the absorption cross-sections of propofol and acetone for UV light. While the absorption of acetone is two orders of magnitude smaller than that of propofol, its concentration in the breath is expected to be higher by a similar order.

To combat the above challenges, the differential detector [4] concept sketched in Figure 1(b) is proposed. The gas sample flows through the detector at a rate of $\approx 50\,\mathrm{cm}^3/\mathrm{min}$, entering first the upper resonator and leaving the cell through the bottom branch. To reduce the cross-talk between the resonators, they are connected by a quarter-wavelength ($\lambda/4$) acoustical filter. The microphones are connected to the resonators by short teflon tubes. The two resonator branches are illuminated by two different wavelengths of light, 275 and 295 nm. The first longitudinal eigenmode of the cylindrical resonators is excited. As shown in Figure 1(a), both trace gases have significant absorption at 275 nm, while at 295 nm only acetone has a high absorption. Thus, the concentration of both species can be attained by a differential evaluation of the two microphone signals. In the sequel, the optical and acoustical design of a detector relying on the above concept is discussed.

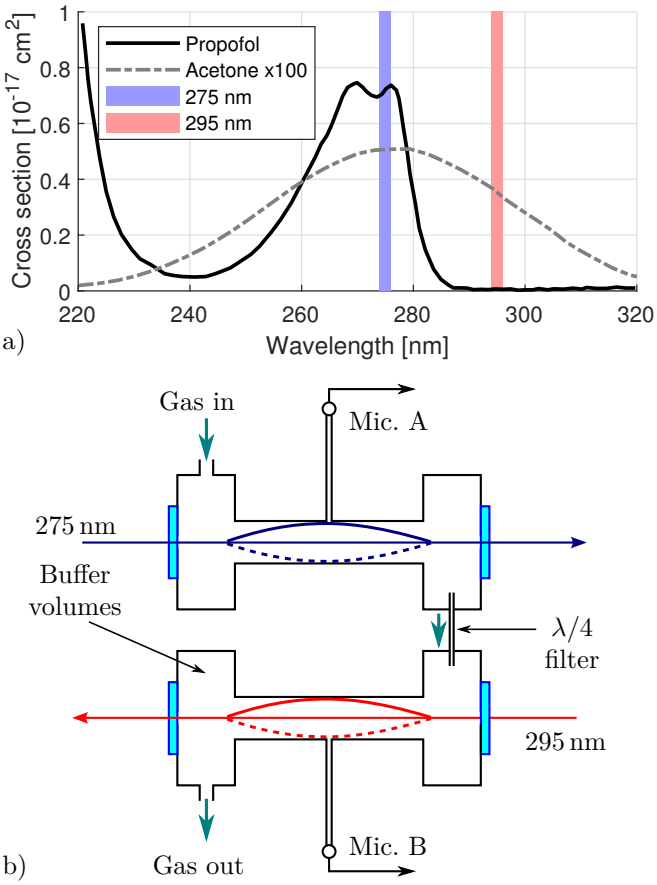


**Figure 1:** Differential detection of propofol and acetone using UV light. a) Absorption cross sections, data from [3]. b) Conceptual sketch of a differential cell with two resonators.

## Optical system

UV LEDs provide an affordable substitute for lasers in many PA applications. These light sources can produce up to a few hundred mW optical power in continuous wave operation. The drawback of LEDs compared to lasers is that they do not emit a collimated beam, and

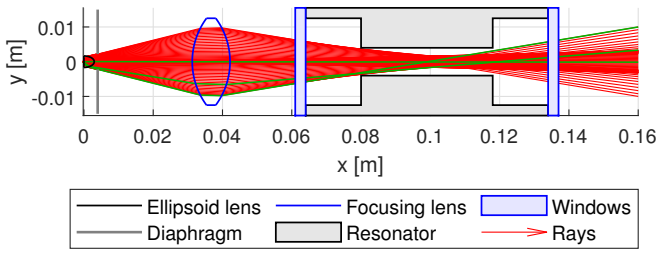


**Figure 2:** Ray tracing simulation of an optical system based on a UV LED with a half-ellipsoid lens.

hence, further optical elements are necessary for guiding their light through a straight resonator.

To be able to simulate the optical system, geometrical ray tracing was applied using an in-house software tool. Rays emitted by directional sources are propagated, reflected, and transmitted at surfaces defined by geometrical primitives (e.g. plane polygons, ellipsoids, cones). Each emitted ray carries a fraction of the light power emitted by the source. Refraction at interfaces is calculated by Snell's law.

Figure 2 shows a light beam formed by an UV LED having a half-ellipsoid lens and a focusing lens. While the LED chip emits rays at a cone angle of ±75°, the half-ellipsoid lens (refraction index $n = 1.49$) reduces the angle to ±15°. A circular diaphragm can be utilized for further narrowing the beam, at the cost of sacrificing some of the light power. By means of the focusing lens ($n = 1.4$) a narrow beam can be formed which can pass through the cylindrical resonator and the buffer volumes. The appearance of the typical double-cone beam pattern is explained by the rays highlighted in green color.

## Finite element model

### Photoacoustic excitation

The heat generated by the absorption of light appears as a spatially distributed source on the right hand side of the wave equation [1]:

$$\frac{1}{c^2}\frac{\partial^2 p(\boldsymbol{x},t)}{\partial t^2} - \nabla^2 p(\boldsymbol{x},t) = \frac{\gamma-1}{c^2}\frac{\partial H(\boldsymbol{x},t)}{\partial t}, \qquad (1)$$

where $\boldsymbol{x}$ and $t$ denote the spatial and time coordinates, $p$ is the sound pressure, $H$ is the heat source, $c$ is the speed of sound, and $\gamma$ is the ratio of specific heats.

To be able to compute $H$ in the FE model, the distribution of the light intensity over the elements of the mesh must be known. As the gas molecules absorb light in the whole volume, the direction of the light rays does not influence the absorption, and hence only the magnitude of the light intensity needs to be evaluated.

The computation is performed following the illustration shown in Figure 3. The average magnitude of the light intensity $q_e$ in element $e$ is found as

$$q_e = \frac{1}{V_e}\sum_{j=1}^{N} l_{ej} w_j, \qquad (2)$$

where $V_e$ is the volume of the element, $N$ is the number of rays, $w_j$ is the light power contained in the $j$th ray,

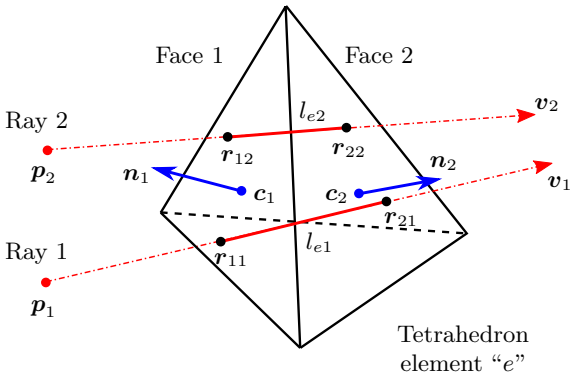


**Figure 3:** Computation of the light intensity magnitude resulting from an optical ray tracing simulation in a tetrahedron element of the acoustical finite element mesh.

and $l_{ej}$ is the distance traveled by ray $j$ in element $e$. For the whole mesh, the intensity magnitudes are gathered in the vector $\mathbf{q}$:

$$\mathbf{q} = \mathbf{V}^{-1}\mathbf{D}\mathbf{w}, \qquad (3)$$

with $\mathbf{V}$ denoting a diagonal matrix that contains the volume of each element of the mesh. The elements of the sparse matrix $\mathbf{D}$ are found as

$$D_{ej} = \sum_{i|e} \operatorname{sgn}(\cos\theta_{ij}) d_{ij}. \qquad (4)$$

The subscript $i|e$ in the summation indicates that the sum is performed over the faces $i$ that belong to element $e$. The angle of incidence is denoted by $\theta_{ij}$, and $d_{ij} = |\boldsymbol{r}_{ij} - \boldsymbol{p}_j|$ is the distance from the starting point of the ray to the intersection point. Note that the sign of $\cos\theta_{ij}$ is positive for a light ray exiting the element, and negative for light rays entering the element; hence, the sum results in the distance traveled by ray $j$ in element $e$. As very small concentrations are considered, the decrease of light power due to absorption is neglected.

### Modeling wall losses

As the photoacoustic cell is a closed volume, the most important losses are those resulting from friction and heat exchange at the walls, represented by the boundary layers with thicknesses $\delta_v$ and $\delta_t$:

$$\delta_v = \sqrt{\frac{2\eta}{\omega\rho_0}} \qquad \delta_t = \sqrt{\frac{2\kappa}{\omega\rho_0 C_p}}, \qquad (5)$$

with $\eta$, $\rho_0$, $\kappa$, and $C_p$ denoting the dynamic viscosity, equilibrium density, thermal conductivity, and the specific heat at constant pressure, respectively.

Berggren *et al.* [5] proposed an approach that enables treating the boundary layers as boundary conditions (BC) in the FE model. For the simulation domain $\Omega$, (1) is transformed into the frequency domain, and for the walls $\Gamma_\mathrm{w}$ the BC is written as:

$$\nabla^2 p + \frac{\omega^2}{c^2} p = -\mathrm{j}\omega\frac{\gamma-1}{c^2} H \qquad \text{in } \Omega \qquad (6)$$

$$-\delta_v' \nabla_T^2 p + \frac{\omega^2}{c^2}\delta_t' p + \frac{\partial p}{\partial n} = 0 \qquad \text{on } \Gamma_\mathrm{w} \qquad (7)$$

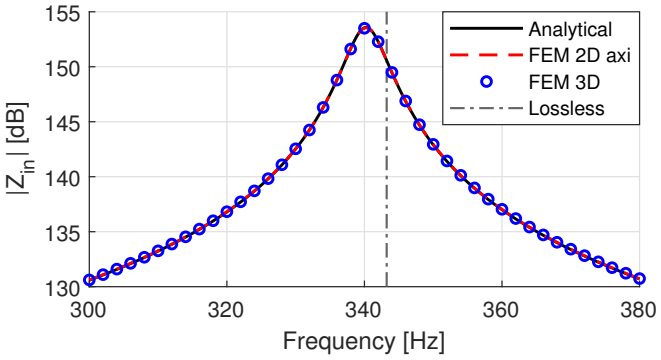


**Figure 4:** Input impedance of a straight cylindrical tube ($L = 500\,\mathrm{mm}$, $r = 10\,\mathrm{mm}$) with wall losses.

where $\delta_v' = \frac{1}{2}(\mathrm{j}-1)\delta_v$ and $\delta_t' = \frac{1}{2}(\mathrm{j}-1)(\gamma-1)\delta_t$, with j being the imaginary unit. The operator $\nabla_T$ denotes the gradient vector containing only the tangential components. To make the problem well-posed a natural BC on $\partial\Gamma_\mathrm{w}$ is also required:

$$\boldsymbol{n}_T \cdot \nabla_T p = 0 \qquad \text{on} \quad \partial\Gamma_\mathrm{w}, \tag{8}$$

with $\boldsymbol{n}_T$ denoting the normal vector that is aligned in the tangential direction of $\Gamma_\mathrm{w}$.

By substituting (7) into the weak form of (6) and performing an integration by parts on $\Gamma_\mathrm{w}$, the following discretized form is attained after applying the standard Galerkin method:

$$\left(\mathbf{K} + \delta_v'\mathbf{K}_\mathrm{w}\right)\mathbf{p} - \omega^2\left(\mathbf{M} - \delta_t'\mathbf{M}_\mathrm{w}\right)\mathbf{p} = -\mathrm{j}\omega\beta(\gamma-1)\mathbf{MAq}, \tag{9}$$

where $\mathbf{K}$ and $\mathbf{M}$ and the mass and stiffness matrices, $\mathbf{K}_\mathrm{w}$ and $\mathbf{M}_\mathrm{w}$ are stiffness and mass contributions of the boundary layers on $\Gamma_\mathrm{w}$ from (7), and $\mathbf{A}$ is a sparse matrix that interpolates from cell centers to the nodes of the mesh. The vector of the pressure coefficients is denoted by $\mathbf{p}$. The coefficient $\beta$ is found as

$$\beta = \alpha N_\mathrm{L} C, \tag{10}$$

where $\alpha$ is the absorption cross-section of one molecule, $N_\mathrm{L}$ is the number of molecules per unit volume, and $C$ is the (dimensionless) concentration of the trace gas.

As a test problem, the input impedance of a straight cylindrical tube with a length $L = 500\,\mathrm{mm}$ and an inner radius $r = 10\,\mathrm{mm}$ is considered. On the input end a rigid piston excites the air column inside the tube, while the other end of the tube has a perfectly rigid termination. Figure 4 depicts the input impedance of the tube computed by the FE method (2D axisymmetric and 3D models) compared to the analytical solution. As it is seen, an almost perfect match is attained. As expected, wall losses also result in a decrease of the resonance frequency compared to the lossless case.

### Optimization of the geometry

While the dimensions of the resonator are strictly constrained by the achievable beam width, there is some freedom in choosing the size of the buffer volumes. An axisymmetric FE model was created which allowed varying

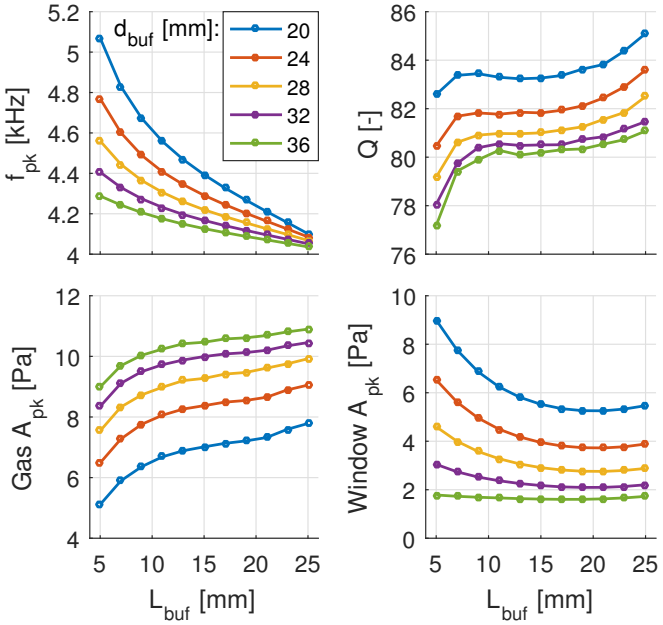


**Figure 5:** Effects of changing the size of the buffer volumes.

the length $L_\mathrm{buf}$ and the diameter $d_\mathrm{buf}$, and both photoacoustic and window signals were simulated. In the latter case, the excitation in (9) was chosen as a uniform normal velocity BC on the intersections of the inner surfaces of the windows and the light beam.

Figure 5 shows the results of the simulations. As visible in the top two diagrams, the size of the buffers slightly affects both the resonance frequency $f_\mathrm{pk}$ and the quality factor $Q$. Interestingly, increasing the length or the diameter of the buffer volumes results in an increase of the magnitude of the useful gas signal (bottom left diagram) and a simultaneous decrease of the window signal (bottom right). This result can be explained by increasing the impedance mismatch between resonator and buffer by increasing the buffer diameter $d_\mathrm{buf}$, and increasing the distance between the excitation and the microphone by increasing the length $L_\mathrm{buf}$.

Having minimal cross-talk between the resonator branches is of key importance for the differential measurement. In order to minimize the cross-talk, the length of the acoustical filter separating the resonators is tuned to $\lambda/4$. Furthermore, decreasing the diameter of the filter was found to be efficient for reducing the cross-talk. Filter diameters 3, 2, and 1 mm resulted in cross-talks of $-29.3$, $-36.3$, and $-48.6\,\mathrm{dB}$, respectively. This result also highlights the importance of the correct treatment of wall losses in the FE model: increasing the amount of viscothermal losses in the filter reduces the undesirable cross-talk of the resonators.

## Comparison with measurements

The PA cell was manufactured and measured in the laboratory at room temperature using 500 ppm acetone in $\mathrm{N_2}$. Figure 6 shows the result of a stepped frequency scan using the 275 nm LED. The box plots display the mean, extrema and quartiles of the measured magnitudes at each testing frequency together with the resonance curve fit-

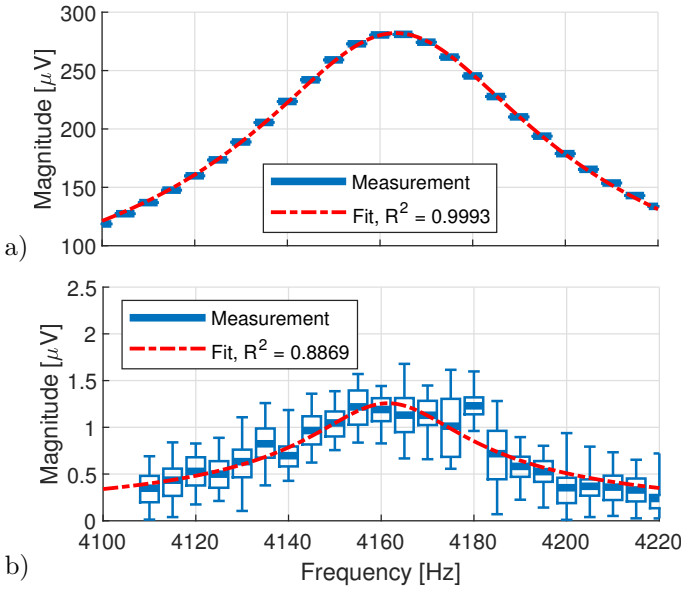


**Figure 6:** Laboratory measurement of cell response and cross-talk using 500 ppm acetone in $N_2$. a) Response in excited branch (275 nm). b) Response in the other branch.

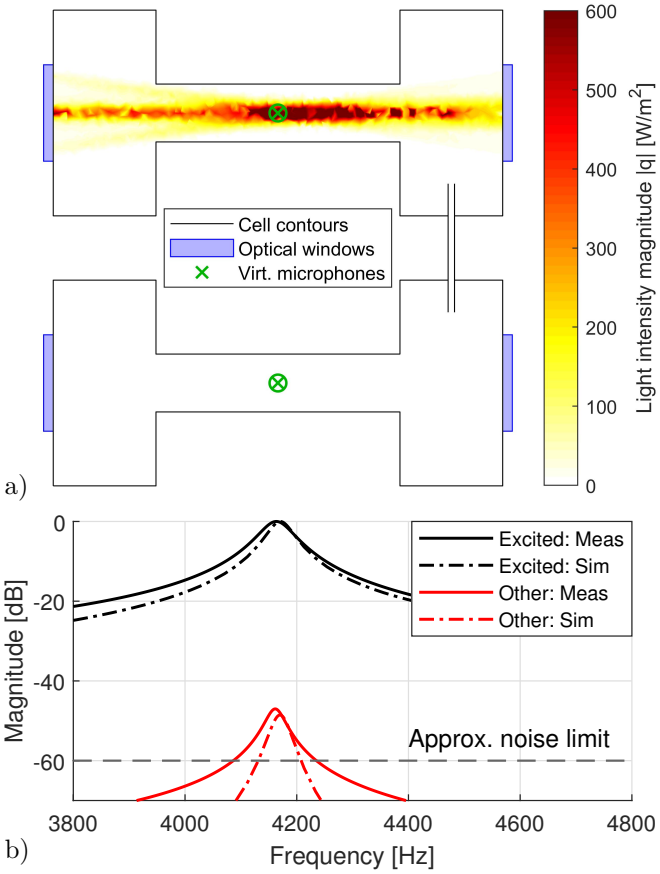


**Figure 7:** Cross-talk measurement and simulation. a) Simulation arrangement and light intensity distribution in the cell. b) Comparison of simulation and measurement results.

ted onto the results. Figure 7 compares the measured and simulated resonance curves in both resonator branches. For the non-excited branch, the measured curve is significantly wider than the simulated one, which is attributed to the measurement noise affecting the fitted curve.

| | Simulation | Measurement |
|---|---|---|
| Resonance freq. ($f_{pk}$) [Hz] | 4 171 | 4 163 |
| Quality factor ($Q$) [–] | 77 | 70 |
| Cross-talk [dB] | −48.6 | −47.0 |

**Table 1:** Comparison of measured and simulated resonance properties of the differential PA cell.

The sensitivity of the cell for 500 ppm acetone was also estimated using the absorption data shown in Figure 1(a). Based on light power measurements, the optical power contained in the light beam passing through the resonator was taken as 5 mW. Assuming a nominal microphone sensitivity of −22 dBV/Pa, the simulation predicts a signal magnitude of 480 $\mu$V, while the measured value is 280 $\mu$V. It is noted that the FE model does not yet contain the microphone tubes or the electro-acoustic model of the microphones. The achieved sensitivity is in good correspondence with the recent UV LED measurements of Weigl *et al.* [6], where a sensitivity of 0.94 $\mu$V/ppm was reported for acetone in $N_2$.

Finally, the comparison presented in Table 1 highlights the applicability and usefulness of virtual prototyping the PA cell using the proposed FE-based techniques.

## Acknowledgments

The contributions of Zlatko Dubovski (cell manufacturing, electrical components) are gratefully acknowledged. This work was supported by the BMBF–VIP+ Project “Photofol” (Ref. Nr.: 03VPO7501).

## References

[1] A. Rosenzwaig. *Photoacoustics and photoacoustic spectroscopy*. John Wiley & Sons, New York, 1980.

[2] C. Hornuss, S. Praun, J. Villinger, A. Dornauer, P. Moehnle, M. Dolch, E. Weninger, A. Chouker, C. Feil, J. Briegel, M. Thiel, and G. Schelling. Real-time monitoring of propofol in expired air in humans undergoing total intravenous anesthesia. *Anesthesiology*, 106(4):665–674, 2007.

[3] T. Laurila, T. Sorvajärvi, J. Saarela, J. Toivonen, D. W. Wheeler, L. Ciaffoni, G. A. D. Ritchie, and C. F. Kaminski. Optical detection of the anesthetic agent propofol in the gas phase. *Analytical Chemistry*, 83:3963–3967, 2011.

[4] A. Miklós, P. Hess, and Z. Bozóki. Application of acoustic resonators in photoacoustic trace gas analysis and metrology. *Review of Scientific Instruments*, 72:1937–1955, 2001.

[5] M. Berggren, A. Bernland, and D. Noreland. Acoustic boundary layers as boundary conditions. *Journal of Computational Physics*, 371:633–650, 2018.

[6] S. Weigl, F. Feldmeier, R. Bierl, and F.-M. Matysik. Photoacoustic detection of acetone in $N_2$ and synthetic air using a high power UV LED. *Sensors and Actuators B: Chemical*, 316:128109, 2020.